Strong-Field Tunneling from a Coherent Superposition of Electronic States

Lutz Fechner,[1,*] Nicolas Camus,[1] Joachim Ullrich,[1,2] Thomas Pfeifer,[1] and Robert Moshammer[1,†]
[1]Max-Planck-Institut für Kernphysik, Saupfercheckweg 1, 69117 Heidelberg, Germany
[2]Physikalisch-Technische Bundesanstalt, Bundesallee 100, 38116 Braunschweig, Germany
(Received 12 February 2014; published 27 May 2014)

Laser-induced tunnel ionization from a coherent superposition of electronic states in Ar^+ is studied in a kinematically complete experiment. Within a pump-probe scheme a spin-orbit wave packet is launched through the first ionization step from the neutral species. The multielectron coherent wave packet is probed as a function of time by the second pulse which ionizes the system to Ar^{++}. By measuring delay-dependent electron momentum distributions we directly image the evolution of the nonstationary multielectron wave function. Comparing the results with simulations we test common assumptions about electron momentum distributions and the tunneling process itself.

DOI: 10.1103/PhysRevLett.112.213001 PACS numbers: 32.80.Fb, 33.60.+q, 42.50.Hz, 82.53.Hn

Electron tunneling is a key ionization mechanism for atoms and molecules exposed to strong laser fields [1–3]. It has been investigated and characterized in numerous experiments, ranging from studies of intensity-dependent ionization rates [4] to measurements of electron momentum distributions [5–7] and streaking experiments [8]. In general, strong-field ionization is interpreted as the tunneling of a bound electron through the potential barrier that is formed by the combined atomic Coulomb and the laser electric field. Once the electron is set free, its motion is dominated by the interaction with the laser field even though modified by the long-range ionic Coulomb potential, which both may lead to various postionization effects [9,10]. Both steps, tunneling and field acceleration, are intrinsically entangled, preventing an unambiguous investigation of the isolated tunneling process itself. Nonetheless, many modern powerful techniques, such as electron streaking [11] and the recently established attoclock principle [12] rely on a well-defined relation between the final (measured) electron momentum and the phase of the laser wave at the moment of tunneling. This relation, however, which usually is acquired from semiclassical calculations, is strongly dependent on the electron velocity right after tunneling.

In this Letter we report on measurements using a coherent superposition of states in Ar^+ as a dynamic initial electronic state subject to further tunneling ionization to Ar^{++}. We present electron momentum distributions for both steps of the sequence and study the delay dependence of the second ionization step. We find a clear dependence on the initial electronic state, extract information about the tunneling process, and image the multielectron wave function in the ion by comparing the results to simulations.

For the longitudinal momentum distribution, along the laser polarization axis, the acceleration of the electron is the dominant factor. It leads to a significant broadening and modification of the initial momentum distribution of the unperturbed electrons appearing in the continuum right after tunneling [13]. A common assumption widely used for simulations is a vanishing longitudinal velocity directly after tunneling (e.g., [9,14,15]) while also other hypotheses were stated, e.g., a velocity distribution of finite width (e.g., [16,17]) or a dependence on the bound-state momentum distribution [18]. For the transverse momenta, perpendicular to the polarization, the situation is substantially different. As the electron does not experience any laser acceleration in this direction, the measured distribution is influenced only by the Coulomb interaction of the ejected electron with its parent ion. Thus, it is expected that the measured momentum reflects to some extent the initial momentum spectrum right after tunneling. Based on early results ([13,19] and references therein) the momentum distribution in strong field ionization neglecting the Coulomb interaction was recently predicted to be a direct image of the bound-state momentum [7,18,20–22]: The atomic wave function in momentum space—in the following $\tilde{\psi}_{(n,l,)m}$ with magnetic quantum number m—is projected onto the continuum by the tunneling process. The latter acts at the same time as a "filter" that suppresses ionization at large momenta. This leads to a transverse momentum distribution of [7]

$$W_{\perp}^{m}(p_{\perp}) = |\tilde{\psi}_{m}(p_{\perp})|^2 \exp\left(-\frac{\sqrt{2E_i}}{F}p_{\perp}^2\right). \quad (1)$$

Here, E_i is the ionization potential, F the laser electric field, and $p_{\perp}$ the electron momentum along a Cartesian coordinate perpendicular to the laser polarization axis, the axis of quantization. The exponential term represents the Gaussian-shaped filter with an intensity-dependent width that arises from standard tunneling theory [13,19]. Though this equation is frequently used for the interpretation of experimental findings [6,7,20], it has never been verified explicitly in any experiment to the best of our knowledge.

In the experiment we use pairs of identical ultrashort (≈ 7 fs), intense ($\approx 5 \times 10^{14}$ W/cm^2) and linearly polarized laser pulses at a central wavelength of 790 nm in a pump-probe scheme. Single laser pulses are created by a commercial Ti:sapphire laser with subsequent spectral broadening in a neon-filled hollow fiber and chirped-mirror pulse compression. By passing a beam splitter and a piezocontrolled Mach-Zehnder interferometer, pulse pairs with an adjustable time-delay τ are produced. The pulses are focused onto a dilute beam of argon atoms provided by a supersonic gas jet inside a reaction microscope. The pressure in the chamber is on the order of 10^{-11} mbar resulting in a very low level of background signals. This is crucial for the two- and three-particle coincidence measurements performed here. The laser polarization is parallel to the weak electric (≈ 2 V/cm) and magnetic fields (≈ 600 μT) that are used to guide the charged particles (ions and electrons) onto time- and position-sensitive detectors. The spectrometer provides kinematically complete data with an electron momentum resolution of about $\Delta p_\perp = 0.02$ a.u. for the transverse and $\Delta p_\parallel = 0.01$ a.u. for the longitudinal component, respectively [atomic units (a.u.) are used unless otherwise stated]. The technical details are given elsewhere [23]. The laser pulse intensity is determined from the width of the measured longitudinal momentum distribution of Ar^+ ions [13,19].

In the data analysis we exclusively use events where all charged particles, e.g., an Ar^{++} ion and two electrons, are recorded in coincidence. This further reduces possible contributions from false coincidences by requiring conservation of the particles' sum momentum. The momentum distribution arising from the first step of the sequence, $Ar \rightarrow Ar^+$, is obtained from electrons measured in coincidence with Ar^+. To determine the electron momentum distribution for the second step, $Ar^+ \rightarrow Ar^{++}$, we first create the spectrum that contains both electrons registered in coincidence with Ar^{++}. Afterwards, we subtract the measured distribution for the single ionization of neutral $Ar \rightarrow Ar^+$.

A time-dependent dynamical initial state is created by launching a multielectron wave packet in the Ar^+ ion for further tunneling. As it was shown theoretically [22,24] and demonstrated experimentally [25–27] this can be achieved by ionizing neutral Ar with a short and strong laser pulse delivered in our experiment by the first pump pulse which also decouples the atomic states. Ionization from the spin-orbit decoupled orbital with $m = 0$ dominates [3] and, therefore, we neglect ionization from other orbitals. After the pump pulse is over, and after projection onto the appropriate spin-orbit coupled eigenstates in the field-free environment, the two lowest coupled states $P_{1/2}$ and $P_{3/2}$ of the Ar^+ ion are coherently populated resulting in a spin-orbit wave packet (SOWP) that evolves in time with a period of $T \approx 23.3$ fs [22,25]. Because of the absence of allowed decay channels, this oscillation is extremely stable and could recently be observed even after nanoseconds [25]. If the removed electron is interpreted as a hole in the electronic shell initially aligned along the laser polarization [22,24], one-particle equations can be used to describe the dynamical evolution of the Ar^+ target. The probability to find the hole in the $m = 0$ orbital after a time delay τ is then to good approximation given by [22,28]

$$P_{m=0}(\tau) = \frac{5}{9} + \frac{4}{9}\cos\left(\frac{\Delta E}{\hbar}\tau\right). \quad (2)$$

Here, $\Delta E \approx 0.1775$ eV [29] is the energy difference between the two states ($P_{1/2}$ and $P_{3/2}$). Directly after the creation of the SOWP and at full periods, only one of the five remaining valence electrons is in the $m = 0$ orbital, while at half periods the electron occupation reaches a value of 17/9. Thus, by choosing the time delay τ, the electronic structure of the target can be controlled and the electron population in the $m = 0$ orbital changes within this range. As a consequence of the dominating ionization from the $m = 0$ orbital a high Ar^{++} yield is obtained at delays $\tau = (i + 1/2)T$, where the electron density in this orbital is at its maximum. As a function of the pump-probe delay time, the yield follows a sinusoidal oscillation with period T [22,25] which is reflecting the hole dynamics. Here, we utilize the oscillation to obtain the phase of the created SOWP and to get information about the shape of the Ar^+ orbital in the moment of second ionization. The chosen intensity is on one hand high enough to ensure that double ionization of Ar takes place in a sequential process [30] (Keldysh parameter $\gamma \approx 0.7$ [1,10] for the second step justifying the tunneling picture). On the other hand, atoms are at most singly ionized by the pump pulse. In fact, a double to single ionization ratio of only about 8%, integrated over all time delays τ, was observed.

Figure 1 shows the measured Ar^{++} yield as a function of τ together with a sinusoidal fit to the data. The slow oscillation of $T \approx 23.3$ fs results from the electronic dynamics in Ar^+ created by tunnel ionization in the first pulse, probed by further ionization to Ar^{++} in the second pulse. Only the temporal region in which the pulses are not overlapping is analyzed. However, optical-cycle (≈ 2.8 fs) interference structures caused by the pulse's pedestals are still visible.

The transverse momentum distribution for ionization of the dynamical Ar^+ target can be calculated using the time-dependent relative occupations of the orbitals and the corresponding theoretically predicted distributions [22], Eq. (1). For our simulation we use Ammosov-Delone-Kraĭnov-ionization rates [3] γ_m with an effective charge $Z^* = \sqrt{2E_i}n$ to calculate the delay-dependent ionization yields. Utilizing Z^* instead of an effective main quantum number n^* (as done, e.g., in [3]) scales the absolute rates by a common factor but preserves the relative ratios. In fact, $\gamma_{m=0}/\gamma_{|m|=1} = 2Z^{*3}/Fn^3 = 2(2E_i)^{3/2}/F$ [3] only depends

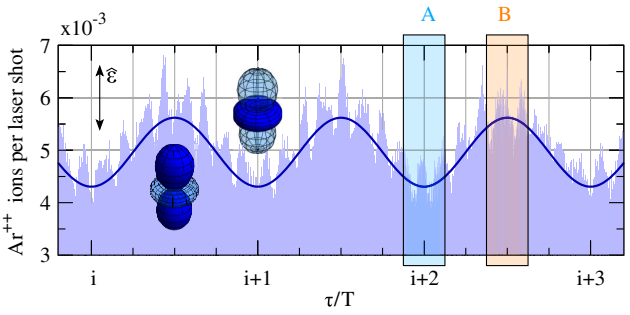

FIG. 1 (color online). Delay-dependent yield of Ar^{++} unveiling the SOWP dynamics in Ar^{+} together with a sinusoidal fit to the data (solid line). Spikes arise from optical interferences with pulse pedestals. The yield maximizes for maximum occupation in the $m = 0$ state as sketched by light and dark blue orbitals in the insets (vertical laser polarization $\hat{\varepsilon}$).

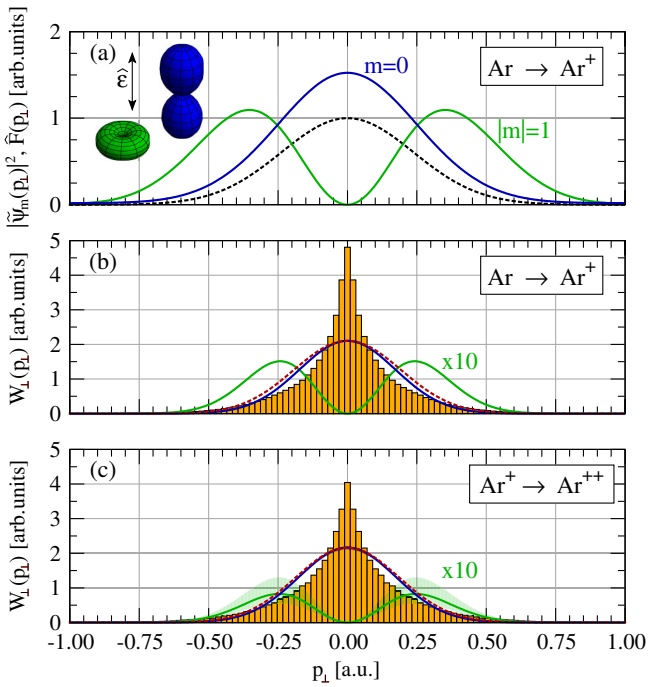

FIG. 2 (color online). (a) The squared wave functions projected onto the transverse momentum axis (solid lines) and the filter term $\hat{F}(p_\perp)$ (dashed line) from Eq. (1) for the first ionization step of neutral Ar. (b) Symmetrized experimental electron momentum distribution $W_\perp(p_\perp)$ (bars) and theoretical prediction (red dashed curve). In addition, the relative contributions of the individual orbitals $W_\perp^m$ are plotted [color code as in (a)]. The $W_\perp^{|m|=1}$ part is multiplied by 10 for better visibility. (c) Same as (b) for the second ionization step. Here, the contributions of the different orbitals are time dependent. The experimental data are averaged over all recorded cycles of the SOWP; corresponding theoretical distributions are shown as solid lines. The light green areas indicate the expected variation as a function of τ. For the $m = 0$ contribution (blue curve) and the total yield (red dashed curve) the latter is barely visible.

on the ionization potential and the field strength of the laser. The actual quantum number $n = 3$ is also consistently used to compute Eq. (1) with Z^*-scaled hydrogenic wave functions in momentum space [31]. Alternatively, a scaling using Slater's rules [32] or numerically obtained values for the effective charge [33] as done, e.g., in [20] would also be possible. To keep consistency within our model calculation and to reproduce the correct ionization potential in the hydrogenic picture we use Z^* as described above. The projections of the squared wave functions and the Gaussian-shaped filter function [see Eq. (1)] for the first ionization step, $Ar \rightarrow Ar^+$, are shown in Fig. 2(a).

The measured momentum distributions $W_\perp(p_\perp)$ are shown in Figs. 2(b) and 2(c). They are obtained after integration of all longitudinal electron momenta. In addition, the theoretical curves for the total signal as well as the contributions from different orbitals are plotted. For the second ionization step, starting from a coherent superposition of states in Ar^+, the theoretically predicted contributions from different orbitals, and thus the widths of the distributions, change slightly with the time-delay τ. Because of the preferential ionization from the $m = 0$ orbital and the relatively narrow filter function the overall distributions are almost Gaussian-like with slight deviations due to the shape of the initial electronic states [light green areas in Fig. 2(c)]. The experimental data presented here are averaged over all recorded cycles of the SOWP. At first glance, the disagreement with theory is striking. While the experimental data show sharp cusplike peaks at zero momentum, an almost Gaussian-shaped distribution is obtained from theory. This behavior has been observed before for ionization of noble gases by intense, linearly polarized laser fields [5]. The attractive Coulomb interaction between the outgoing electron and the parent ion, which is not included in the present theory, causes a significant modification of the transverse momentum distribution with a focusing of events at zero momentum. Very similar cusp-dominated electron spectra are observed in ionizing ion-atom collisions at very high energies [34,35]. There it was also shown that the shape of the atomic bound-state momentum distribution is imprinted, at least partly, in the momentum spectrum of the ionized electrons. In the following we will elucidate the question whether the same holds true for the case of strong-field ionization and whether the predicted influence of the bound-state wave function $\tilde{\psi}$ [see Eq. (1)] on the electron momentum distribution can be observed despite the final-state Coulomb interaction.

In the theoretical model, neglecting the Coulomb interaction, the width of the transverse momentum distribution depends on (i) the shape of the bound-state wave function in momentum space, (ii) the relative contributions from the different orbitals, and (iii) the width of the Gaussian filter function. Considering an ionic target Ar^+ compared to neutral Ar, (i) broadens the distribution while (ii) and (iii) are compensating for this effect. In order to visualize the expected small variations in the electron momentum

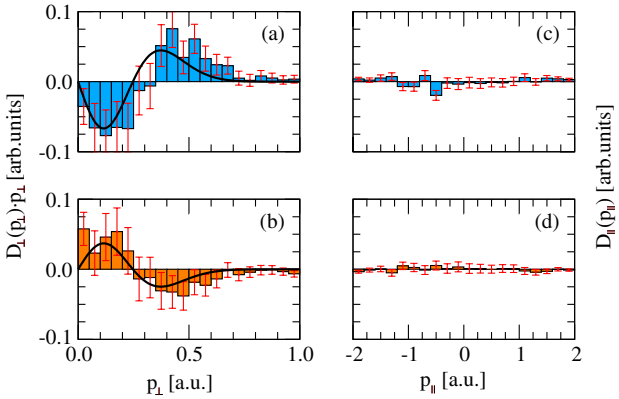

FIG. 3 (color online). (a) and (b) Experimental transverse momentum distributions after subtraction of the time-averaged distribution [$D_\perp(p_\perp,\tau)$ of Eq. (3), see text] for two delay times (windows A and B from Fig. 1). Black solid lines denote the theoretical results for the corresponding time delays $\tau = iT$ and $\tau = (i+1/2)T$, respectively. (c) and (d) Corresponding spectra $D_\parallel(p_\parallel,\tau)$ for the longitudinal electron momenta.

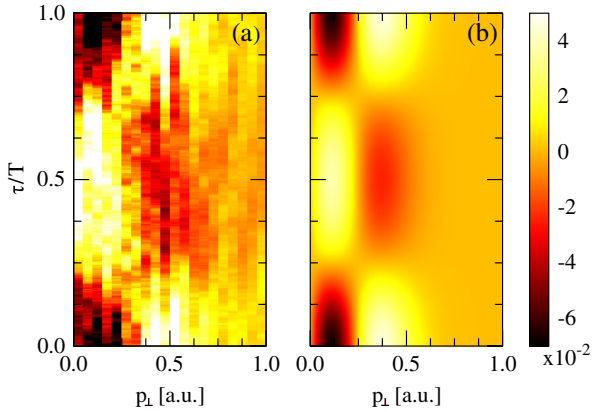

FIG. 4 (color online). 2D presentation of the transverse momentum distribution after subtraction of the time-independent part $D_\perp(p_\perp,\tau)$ as a function of momentum $p_\perp$ and delay τ (left: experiment, right: theory).

spectrum caused by the SOWP dynamics in Ar^+, we subtract the measured time-averaged momentum distribution $\bar{W}$ from those obtained at a given time delay after normalizing both:

$$D(p,\tau) = W(p,\tau) - \bar{W}(p). \tag{3}$$

This difference distribution is very sensitive to small changes originating from the bound-state SOWP dynamics. At the same time any contribution from the first ionization step is canceled out since this step does not depend on τ. The largest contrast is expected to appear at time delays where the electron occupation maximizes either in the $m = 0$ or $|m| = 1$ orbital. Therefore, we define two time windows $\tau \pm T/8$ around $\tau = iT$ (window A in Fig. 1) and $\tau = (i+1/2)T$ (window B) and analyze the events therein.

The result for the transverse momenta is shown in Figs. 3(a) and 3(b), where the measured and calculated $D_\perp$ distributions are plotted for the two delay-time windows. In order to increase the statistical significance of the symmetric experimental data we consider the absolute $p_\perp$ values in the following. The theoretical curves are calculated for fixed times at $\tau = T$ and $\tau = T/2$, respectively, whereas the experimental ones are obtained after averaging over the width of the time window. In contrast to the direct comparison in Fig. 2 now the agreement with theory is remarkably good, indicating that the cusplike structure in the $W_\perp(p_\perp)$ distribution, which is not reproduced at all by our model calculation, is effectively suppressed after applying Eq. (3). The agreement is impressive considering the simplicity of our theoretical model, using Ammosov-Delone-Kraĭnov rates with scaled hydrogenic wave functions and neglecting the final-state Coulomb interaction completely. Moreover, the shapes of the calculated distributions depend on the laser intensity. We like to note that a similar behavior, namely, a $\approx 15\%$ disagreement in the momentum widths between experiment and theory, has recently been reported for tunneling ionization of atoms with circularly polarized laser fields [7,20].

The same analysis as for the transverse direction can be done with the longitudinal momentum spectra. The corresponding $D_\parallel$ distributions are shown in Figs. 3(c) and 3(d). In this case no dependence on the delay time is found, indicating that electrons emitted along the field direction do not carry information about the bound-state SOWP dynamics. This result can be explained by an m-independent momentum distribution or even an electron momentum of zero directly after tunneling, in agreement with the common assumption mentioned in the beginning. However, it is also possible that an initially existing m dependence on the momentum distributions is removed by a "bunching" mechanism caused by soft recollisions of the electrons with their parent ion [36].

A more complete view on the initial-state dependence of the transverse momentum distribution in tunneling ionization of SOWP excited Ar^+ is obtained by plotting $D_\perp$ as a function of both momentum and time. The corresponding 2D plots (experiment and theory) are shown in Figs. 4(a) and 4(b). The experimental data are integrated over a time window of $\tau \pm T/8$ with τ now running over one full period of the SOWP while the theoretical expression is evaluated at delays τ without averaging. Cuts along $\tau = T$ and $\tau = T/2$ result in the spectra shown in Figs. 3(a) and 3(b). Again, the initial-state dynamics is clearly visible, and excellent agreement with theory is achieved.

In conclusion, using a reaction microscope for low-background three-particle coincidence measurements in combination with ultrashort, strong laser pulses we studied tunneling ionization of a dynamical target, namely, coherently excited electronic states forming a spin-orbit wave packet in Ar^+. Though the general shapes of the $p_\perp$

distributions are only barely reproduced with the present tunneling model, which does not account for the long-range Coulomb interaction, the initial-state dependence is remarkably well described with the product ansatz of Eq. (1). It is clearly demonstrated that the initial-state momentum distribution is imprinted onto the transverse momentum spectrum of the ionized electrons. Our results and future experiments on strong-field ionization from dynamical states will provide detailed information about the ionization process and, in addition, about the bound-state multielectron dynamics in the ion.

*lutz.fechner@mpi-hd.mpg.de
†robert.moshammer@mpi-hd.mpg.de

[1] L. V. Keldysh, Sov. Phys. JETP **20**, 1307 (1965).
[2] A. M. Perelomov, V. S. Popov, and M. V. Terent'ev, Sov. Phys. JETP **23**, 924 (1966).
[3] M. V. Ammosov, N. B. Delone, and V. P. Kraĭnov, Sov. Phys. JETP **64**, 1191 (1986).
[4] B. Walker, B. Sheehy, L. F. DiMauro, P. Agostini, K. J. Schafer, and K. C. Kulander, Phys. Rev. Lett. **73**, 1227 (1994).
[5] A. Rudenko, K. Zrost, Th. Ergler, A. B. Voitkiv, B. Najjari, V. L. B. de Jesus, B. Feuerstein, C. D. Schröter, R. Moshammer, and J. Ullrich, J. Phys. B **38**, L191 (2005).
[6] M. Meckel, D. Comtois, D. Zeidler, A. Staudte, D. Pavičić, H. C. Bandulet, H. Pépin, J. C. Kieffer, R. Dörner, D. M. Villeneuve, and P. B. Corkum, Science **320**, 1478 (2008).
[7] L. Arissian, C. Smeenk, F. Turner, C. Trallero, A. V. Sokolov, D. M. Villeneuve, A. Staudte, and P. B. Corkum, Phys. Rev. Lett. **105**, 133002 (2010).
[8] R. Boge, C. Cirelli, A. S. Landsman, S. Heuser, A. Ludwig, J. Maurer, M. Weger, L. Gallmann, and U. Keller, Phys. Rev. Lett. **111**, 103003 (2013).
[9] P. B. Corkum, Phys. Rev. Lett. **71**, 1994 (1993).
[10] W. Becker, X. Liu, P. J. Ho, and J. H. Eberly, Rev. Mod. Phys. **84**, 1011 (2012).
[11] R. Kienberger, E. Goulielmakis, M. Uiberacker, A. Baltuska, V. Yakovlev, F. Bammer, A. Scrinzi, Th. Westerwalbesloh, U. Kleineberg, U. Heinzmann, M. Drescher, and F. Krausz, Nature (London) **427**, 817 (2004).
[12] P. Eckle, M. Smolarski, P. Schlup, J. Biegert, A. Staudte, M. Schöffler, H. G. Muller, R. Dörner, and U. Keller, Nat. Phys. **4**, 565 (2008).
[13] N. B. Delone and V. P. Krainov, J. Opt. Soc. Am. B **8**, 1207 (1991).
[14] P. Eckle, A. N. Pfeiffer, C. Cirelli, A. Staudte, R. Dörner, H. G. Muller, M. Büttiker, and U. Keller, Science **322**, 1525 (2008).
[15] C. Liu and K. Z. Hatsagortsyan, Phys. Rev. Lett. **105**, 113003 (2010).
[16] A. N. Pfeiffer, C. Cirelli, A. S. Landsman, M. Smolarski, D. Dimitrovski, L. B. Madsen, and U. Keller, Phys. Rev. Lett. **109**, 083002 (2012).
[17] C. Hofmann, A. S. Landsman, C. Cirelli, A. N. Pfeiffer, and U. Keller, J. Phys. B **46**, 125601 (2013).
[18] M. Y. Ivanov, M. Spanner, and O. Smirnova, J. Mod. Opt. **52**, 165 (2005).
[19] N. B. Delone and V. P. Krainov, Phys. Usp. **41**, 469 (1998).
[20] I. Dreissigacker and M. Lein, Chem. Phys. **414**, 69 (2013).
[21] M. Spanner, O. Smirnova, P. B. Corkum, and M. Y. Ivanov, J. Phys. B **37**, L243 (2004).
[22] H. J. Wörner and P. B. Corkum, J. Phys. B **44**, 041001 (2011).
[23] J. Ullrich, R. Moshammer, A. Dorn, R. Dörner, L. Ph. H. Schmidt, and H. Schmidt-Böcking, Rep. Prog. Phys. **66**, 1463 (2003).
[24] N. Rohringer and R. Santra, Phys. Rev. A **79**, 053402 (2009).
[25] A. Fleischer, H. J. Wörner, L. Arissian, L. R. Liu, M. Meckel, A. Rippert, R. Dörner, D. M. Villeneuve, P. B. Corkum, and A. Staudte, Phys. Rev. Lett. **107**, 113003 (2011).
[26] E. Goulielmakis, Z.-H. Loh, A. Wirth, R. Santra, N. Rohringer, V. S. Yakovlev, S. Zherebtsov, T. Pfeifer, A. M. Azzeer, M. F. Kling, S. R. Leone, and F. Krausz, Nature (London) **466**, 739 (2010).
[27] A. Wirth, M. Th. Hassan, I. Grguraš, J. Gagnon, A. Moulet, T. T. Luu, S. Pabst, R. Santra, Z. A. Alahmed, A. M. Azzeer, V. S. Yakovlev, V. Pervak, F. Krausz, and E. Goulielmakis, Science **334**, 195 (2011).
[28] H. Wen, S. N. Pisharody, J. M. Murray, and P. H. Bucksbaum, Phys. Rev. A **73**, 052504 (2006).
[29] A. Kramida, Yu. Ralchenko, J. Reader, and NIST ASD Team (2013), NIST Atomic Spectra Database (ver. 5.1), [Online]. Available: http://physics.nist.gov/asd [2014, February 10]. National Institute of Standards and Technology, Gaithersburg, MD.
[30] S. Augst, A. Talebpour, S. L. Chin, Y. Beaudoin, and M. Chaker, Phys. Rev. A **52**, R917 (1995).
[31] B. Podolsky and L. Pauling, Phys. Rev. **34**, 109 (1929).
[32] J. C. Slater, Phys. Rev. **36**, 57 (1930).
[33] E. Clementi and D. L. Raimondi, J. Chem. Phys. **38**, 2686 (1963).
[34] P. D. Fainstein, R. Moshammer, and J. Ullrich, Phys. Rev. A **63**, 062720 (2001).
[35] R. Moshammer, P. D. Fainstein, M. Schulz, W. Schmitt, H. Kollmus, R. Mann, S. Hagmann, and J. Ullrich, Phys. Rev. Lett. **83**, 4721 (1999).
[36] A. Kästner, U. Saalmann, and J. M. Rost, Phys. Rev. Lett. **108**, 033201 (2012).